Journal of Materials Science & Technology 206 (2025) 282–296

Contents lists available at ScienceDirect

Journal of Materials Science & Technology

journal homepage: www.elsevier.com/locate/jmst

Research Article

In-situ growth of 3D amorphous Ni-Co-Mn phosphate on 2D $Ti_3C_2T_x$ nanocomposite for commercial-level hybrid energy storage application

Pranav K. Katkar[a], Zulfqar Ali Sheikh[b], Vijay D. Chavan[b], Sang-Wha Lee[a,*]

[a] Department of Chemical and Biological Engineering, Gachon University, 1342 Seongnam-daero, Seongnam-Si 13120, Republic of Korea
[b] Department of Electrical Engineering, Sejong University, Seoul 05006, Republic of Korea

ARTICLE INFO

Article history:
Received 19 January 2024
Revised 25 March 2024
Accepted 26 March 2024
Available online 26 April 2024

Keywords:
Ni-Co-Mn phosphate
$Ti_3C_2T_x$
Electrodeposition
Nanocomposite
Amorphous nature
Hybrid solid-state supercapacitor

ABSTRACT

To overcome the limited electronic conductivity and capacity of single and binary transition metal phosphates (TMPs), highly electrochemical active materials and rational structural design of ternary TMPs composite are urgently required. In this study, we successfully synthesized an amorphous 3D Ni-Co-Mn phosphate@2D $Ti_3C_2T_x$ (MXene) nanocomposite (NCMP series) through the electrodeposition method. The amorphous Ni-Co-Mn phosphate effectively restricts the self-accumulation of MXene nanosheets, resulting in the development of a porous nanostructure. This structure exposes more active sites, expands the ion transport path, and enhances the conductivity of the Ni-Co-Mn phosphate@$Ti_3C_2T_x$ material. Owing to the synergistic effect offered by Ni-Co-Mn phosphate and MXene nanocomposite, the anchored Ni-Co-Mn phosphate@$Ti_3C_2T_x$ (NCMP-5) electrode delivers an elevated capacity of 342 mAh/g (1230 C/g) at 5.0 A/g, surpassing the pristine Ni-Co-Mn phosphate (NCMP-4, 260 mAh/g) and MXene (33.3 mAh/g). Moreover, a hybrid solid-state supercapacitor (HSSC) device is assembled with NCMP-5 as a cathode and reduced graphene oxide (rGO) as an anode within a polymer gel (PVA-KOH) electrolyte. Notably, the fabricated HSSC device displays a supreme specific capacity of 27.5 mAh/g (99 C/g) and a high (volumetric) energy density of 22 Wh/kg (3.6 Wh/cm^3) at a power density of 0.80 kW/kg (0.13 kW/cm^3) for 1.0 A/g. Moreover, the HSSC device retains 95.4 % of its initial capacity even after 10,000 cycles. Importantly, the operational potential window of two serially connected HSSC devices approaches +3.2 V, enabling different colored commercial light-emitting diodes (LEDs) to be efficiently illuminated. Eventually, the remarkable supercapacitive characteristics of the 3D@2D amorphous Ni-Co-Mn phosphate@MXene nanocomposite make it an attractive choice for advanced electroactive materials in upcoming hybrid energy storage technologies.

1. Introduction

To promote the harmonious coexistence of humans and the environment, it is essential to carry out research and development on an innovative kind of green energy resource that may progressively replace the use of fossil fuels [1]. As a result, modern energy storage technologies are being extensively studied in the growing field of sustainable energy development [2]. Among the several modern energy storage technologies, the supercapacitor-battery hybrid system is remarkable, and it is referred to as a “hybrid supercapacitor (HSC)” [3]. It combines the charge storage mechanisms, and advantages of rechargeable batteries and supercapacitors for high power and energy efficiency, which can potentially fill the performance gap between them [4]. In addition, it is suggested that designing an HSC with a wide working voltage range is a successful strategy for high power and energy density [5]. However, owing to the sluggish kinetics and weak reversibility of battery reactions [6], the battery electrode performs poorly in comparison to the supercapacitor electrode during long-term cycling. Hence, the development of high-performance electroactive materials for HSCs is required. To meet this requirement, transition metal phosphates (TMPs) gained the attention of many researchers owing to their remarkable properties, such as improved conductivity compared with metal oxides/hydroxides [7], superior redox activity, stronger P-O covalent bonds, open framework configuration, superb physico-chemical characteristics, and metalloid properties, which provide faster electron transport and cycle efficiency [8,9].

Generally, Individual cobalt and nickel phosphates have a high capacity, but their cyclic stability is quite unsatisfactory [10,11]. On the contrary, manganese phosphate has a much lower capacity but outstanding cyclic stability [12]. To overcome these obstacles, additional metal cations need to be incorporated into

* Corresponding author at: Department of Chemical and Biological Engineering, Gachon University, 1342 Seongnam-daero, Seongnam-si, 13120, Republic of Korea.
E-mail address: lswha@gachon.ac.kr (S.-W. Lee).

https://doi.org/10.1016/j.jmst.2024.03.044
1005-0302/

mono-metallic phosphate. Compared with mono-metal phosphates, the bimetal or tri-metal phosphates with adjustable composition show better performance because of their combined contribution from respective transition metals [13]. Therefore, combining three metals with phosphate can provide more advantages (synergistic effect from several metal ions) than one metal, including abundant crystalline interfaces and multiple redox reactions on surface and cycle performance [14]. However, not much investigation has been conducted so far on the performance of ternary phosphate. This scenario prompted further investigations into the influence of more elements. Nevertheless, there are few reports on ternary materials such as Zn-Ni-Co phosphide achieved a specific capacity of 1269 C/g at 3 A/g [15], and Ni-Co-Mo phosphide exhibited a 508 F/g capacitance value at 0.2 A/g current density [7]. Hence, efficient element selection is critical to ensuring improved electrochemical activity. They are inspired by recent research revealing the beneficial synergistic effects of Ni-Mn [16], Ni-Co [17], and Co-Mn [18], and it appears to be a promising option to improve the electrochemical properties and long-term cyclic stability for a ternary metallic framework. Furthermore, cobalt, nickel, and manganese-based materials are environmentally friendly compounds, relatively cheap, naturally abundant, and have superb electrical conductivity with rich redox chemistry [19,20]. Although this tri-metal phosphate exhibits multiple electroactive sites and facilitates rapid electron/ion transport, accessing all electroactive sites proves challenging, resulting in limited electronic conductivity [21]. Hence, a practical way to substantially improve electrochemical performance is to include different conductive additives and active substrates to obtain high electronic conductivity.

Recently, various 2D layered materials (like graphene, black phosphorus, phosphorene, etc.) have been investigated [22]. Among this variety of 2D materials, MXene ($Ti_3C_2T_x$) has been extensively investigated owing to its robust chemical and surface characteristics, including its high carrier density, ultra-high electronic conductivity (almost the same as layered graphene), considerable specific surface area, rich surface chemistry because of a large number of functionality groups (-F, -O, and -OH), and facile dispersion in different solvents (including water) with significant yields [23]. Furthermore, MXene is a naturally occurring superconductive semi-metal, which relies on surface composition. Additionally, MXene offers conductive networks that avoid aggregation, accelerate electron transmission, and boost electrode cycle durability [24]. It is important to note that the MXene surface is highly electronegative due to the adsorbed surface functional groups, which interact with positive charges to anchor metal cations and give the MXene surface capacity to nucleate with other metal ions [25]. Therefore, MXene is considered a functionalized substrate that can anchor additional chemical components to produce high-performing supercapacitors. MXene-based materials are attractive electrodes due to their low metal diffusion barrier on their surfaces, tunable interlayer spacing, and hydrophilicity [26]. If the synergistic effect of MXene and Ni-Co-Mn phosphate hybrid can be achieved, the conductivity of the material and electrochemical properties would be significantly enhanced. As far as we know, not a single study has been done on the coupling of ternary Ni-Co-Mn phosphate with MXene nanocomposite for the construction of high-performance supercapacitor electrode materials. Moreover, TMPs tend to self-aggregate after multiple charge-discharge cycles or the use of binders, which disclosed limited active sites, lower electrical conductivity, and limited cycle stability [27]. Therefore, if direct TMP growth on substrate surfaces is achieved in a highly porous and well-organized nanostructure, it may encourage TMP conductivity enhancement while preventing the accumulation and agglomeration of active materials [28]. Furthermore, the in-situ growth of electrode material on a conductive substrate has proven to be an effective approach for promoting electrolyte wettability, and electron transport and addressing the issue of low conductivity [29,30]. These concepts serve as inspiration for the in-situ manufacturing of TMP with an adjustable composition and a rational geometric structure on a substrate, which is a useful remedy for the problems mentioned earlier.

Based on the considerations mentioned earlier, we elaborately designed 3D amorphous ternary Ni-Co-Mn phosphate nanoparticles (NPs) on the surface of 2D MXene nanosheets through an in-situ electrodeposition growth method and successfully constructed 3D/2D Ni-Co-Mn phosphate@$Ti_3C_2T_x$ nanocomposite (referred to as NCMP) on a conductive nickel foam (NF) substrate. The developed Ni-Co-Mn phosphate@$Ti_3C_2T_x$ (denoted as NCMP-5) demonstrated exceptional electrochemical performance for supercapacitors, demonstrating a specific capacity (342 mAh/g at 5.0 A/g) and excellent cyclic stability (98.8 %) for 5000 cycles. This outstanding performance may be attributed to the following advantages of the Ni-Co-Mn phosphate@$Ti_3C_2T_x$ composite electrode material: (i) multiple elements offer additional redox-active sites for redox transformations; (ii) the layered stacking arrangement of 2D nanosheets in the $Ti_3C_2T_x$ promotes electrolyte penetration and ion/electron transfer; and iii) the improvement of electrical conductivity and stability of the entire electrode material framework [31]. Moreover, a HSSC device assembled with rGO as anode in PVA-KOH solid gel electrolyte (the HSSC denoted as NCMP-5//rGO) achieved maximum specific capacity with a high (volumetric) energy density of 22 Wh/kg (3.6 Wh/cm^3) at a power density of 0.80 kW/kg and excellent cyclic stability over 10,000 cycles. These outcomes highlight the significant electrochemical performance of a trimetallic 3D/2D amorphous Ni-Co-Mn phosphate@$Ti_3C_2T_x$ nanocomposite, opening a new avenue for research and potential commercial applications in electronics.

2. Experimental section

Synthesis of Ni–Co–Mn phosphate@MXene/NF composite thin films

In this research, the potentiostatic electrodeposition of Ni-Co-Mn phosphate on NF was carried out by employing a ZIVE SP1 Potentiostat. The NF is utilized as the substrate for electrodeposition due to its 3D porous structure and high electrical conductivity, which reduces electrolyte diffusion resistance and promotes the transportation of ions [32]. In this investigation, the different electrodeposition solution baths were prepared by a varied concentration of $NiCl_2{\cdot}6H_2O$, $CoCl_2{\cdot}6H_2O$, and $MnCl_2{\cdot}4H_2O$ with a fixed concentration of KH_2PO_4 (0.20 M) in 80 mL DI water, as specified in Table 1. To prevent the production of oxide/hydroxide, the deposition employed a high composition of phosphate precursor, and Ni, Co, and Mn precursors concentration adjusted based on the material's growth rate. As in the previous protocol [16], the synthesis process used chronoamperometry to perform the potentiostatic electrodeposition. The proposed electrodeposition was performed for 10 min at a potential of −1.0 V in a three-electrode cell arrangement, which consisted of the cleaned NF (1×4 cm^2) serving as the working electrode, a graphite rod as the counter electrode, and silver/silver chloride (Ag/AgCl) as the reference electrode. After the 10 min deposition, the resulting binder-free Ni-Co-Mn phosphate-based electrodes were cleaned with DI water and then dried out at ambient temperature. Based on the composition ratios of Ni, Co, and Mn, the synthesized Ni-Co-Mn phosphate-based electrodes have been referred to as NCMP-1, NCMP-2, NCMP-3, NCMP-4, NCMP-5, and MXene and they are listed in Table 1. Also, the electrodeposition fabricated NCMP thin films with varying Ni/Co/Mn concentrations are depicted in Scheme 1(a, b). After electrodeposition, the mass difference of NF before and after deposition was computed to determine the mass of the deposited material. The standard mass loading of the deposited materials was

Table 1
Different nickel, cobalt, manganese, phosphate, and MXene precursor concentrations and notations for the synthesis of Ni-Co-Mn phosphate/Mxene composite.

Sr. No.	$NiCl_2·6H_2O$ (M)	$CoCl_2·6H_2O$ (M)	$MnCl_2·4H_2O$ (M)	KH_2PO_4 (M)	MXene (mg)	Notations
1	0.10	0.00	0.00	0.20	–	NCMP-1
2	0.00	0.10	0.00	0.20	–	NCMP-2
3	0.00	0.00	0.10	0.20	–	NCMP-3
4	0.033	0.033	0.033	0.20	–	NCMP-4
5	0.033	0.033	0.033	0.20	3.0 mg	NCMP-5
6		–			3.0 mg	MXene

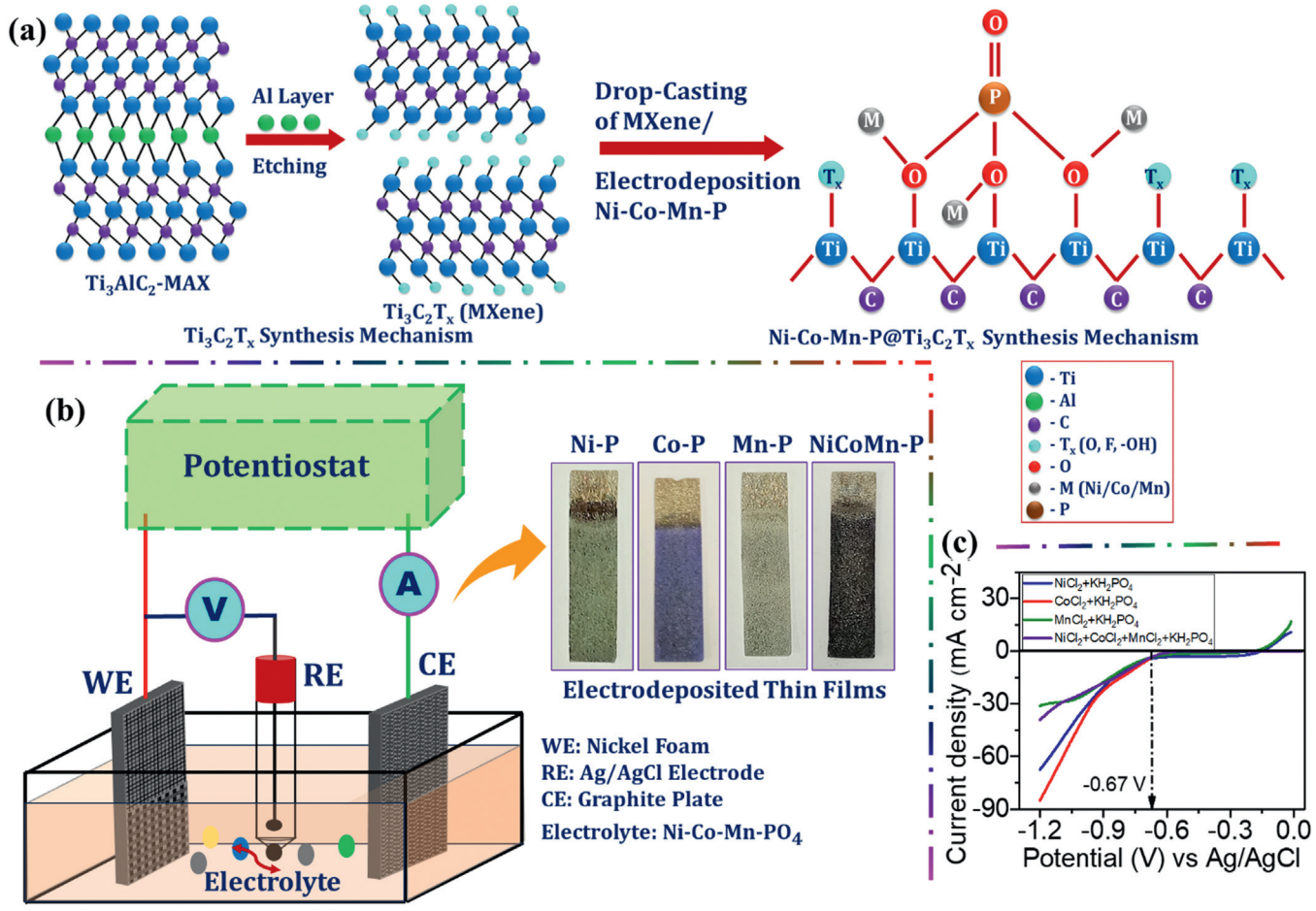

Scheme 1. Schematic of the (a) MXene preparation by Al etching, (b) electrodeposition process for the growth of Ni-Co-Mn phosphate on NF, and (c) LSV curves for the precursor solutions of $NiCl_2$, $CoCl_2$, $MnCl_2$, and $NiCl_2$ + $CoCl_2$ + $MnCl_2$ (with KH_2PO_4) at a sweep rate of 20 mV/s.

2.98, 1.10, 0.81, 1.50, 1.18, and 0.82 mg/cm^2 for NCMP-1, NCMP-2, NCMP-3, NCMP-4, NCMP-5, and MXene, respectively. Ultimately, additional characterization experiments were performed directly on those dried Ni-Co-Mn phosphate@MXene composite-based thin films. However, the structural and electrochemical characterization techniques of all as-prepared samples are included in the supporting information (SI). SI further involves a brief explanation of the anode (rGO) preparation, gel electrolyte preparation, and hybrid solid-state supercapacitor assembly process.

3. Results and discussion

3.1. Formation and reaction mechanism of Ni-Co-Mn Phosphate@MXene composite thin films

In the beginning, the HF etching process was used to manufacture MXene; Scheme 1(a) shows a manifestation of this structural model. Following that, the as-prepared MXene powder was drop-cast onto NF. Besides, the nano-architectured 3D Ni-Co-Mn phosphate on 2D MXene-coated NF (NCMP series) has been synthesized using potentiostatic electrodeposition (Scheme 1(b)). In the NCMP preparation procedure, the charged properties of MXene (negatively) and Ni-Co-Mn phosphate (positively) interfaces attract each other, owing to the columbic electrostatic and van der Waals interactions [16]. Generally, there are three steps of the electrodeposition process as follows: initially, the protective coating was relaxed as the Ni/Co/Mn cations passed via the diffusion layer. Subsequently, electrons are displaced and gathered on Ni foam. Ultimately, cation insertion takes place at a more energetically stable site [14]. In the subsequent preparation procedure, the linear sweep voltammetry (LSV) was scanned at a rate of 20 mV/s from 0.0 to −1.2 V/Ag/AgCl, to display the deposition potential (onset potential). According to this LSV curve, the Mn and Ni-Co-Mn precursor solution exhibits a higher negative re-

duction potential and a smaller current response compared to the separate Ni and Co precursor solutions. Nonetheless, their reduction potentials are nearly identical, hence the same potential for the deposition of uncomplexed ions is used [16]. As a result, a reduction potential of −1.0 V assures the deposition of all metal cations, since the potential of Ni/Co/Mn ions is almost −0.67 V vs. Ag/AgCl, as demonstrated by LSV investigation (Scheme 1(c)). Following that, the solution is reduced, and the reduction current rapidly rises from −0.67 V/Ag/AgCl owing to the initiation of the nucleation process. It appears that the applied reduction voltage (for 10 min) propelled the transfer of Ni^{2+}, Co^{2+}, and Mn^{2+} cations to the NF and then simultaneously reacted with PO_4^{3-} during the electrodeposition process [33]. These ions migrated in a directed manner to form the nanostructure, and it is uniformly distributed and strongly attached to NF after a certain period, leading to the formation of NCMP series electrodes [34]. After electrodeposition (Scheme 1(b)), the color of the NF varied from light green (NCMP-1), violet (NCMP-2), and white (NCMP-3) to dark black (NCMP-4,5). The following equations can be utilized to describe the mechanisms of chemical reactions involved in the formation of Ni-Co-Mn phosphate@MXene electrode:

In electrodeposition, the MXene-coated NF substrate is an electrode (cathode), where reduction reactions occur as follows:

$$Ni^{2+} + 2e^- \rightarrow Ni \quad (1)$$

$$Co^{2+} + 2e^- \rightarrow Co \quad (2)$$

$$Mn^{2+} + 2e^- \rightarrow Mn \quad (3)$$

$$(3-x)Ni^{2+} + (x)Co^{2+} + (x)Mn^{2+} + 2H_2O \rightarrow Ni_{(3-x)}Co_{(x)}Mn_{(x)}(OH)_2 + 2H^+ \quad (4)$$

At the anode (oxidation occurs):

$$2Cl^- \rightarrow Cl_2 + 2e^- \quad (5)$$

Meanwhile, Eq. (6) reveals that KH_2PO_4 dissociates in the presence of metal cations, forming free HPO_4^{2-} ions that serve as the source of phosphate ions.

$$KH_2PO_4 \rightarrow K^+ + HPO_4^{2-} + H^+ \quad (6)$$

Concurrently, the PO_4^{3-} ion replaces the OH^- ion in $Ni_{(3-x)}Co_{(x)}Mn_{(x)}(OH)_2$, and those phosphate ions in the electrolyte interact with Ni, Co, and Mn metallic cations to form $Ni_{(3-x)}Co_{(x)}Mn_{(x)}(PO_4)_2$ on the MXene embellished NF surface, as shown in the following reaction [Eq. (7)] [35]. It is noteworthy that Ni^+, Co^+, and Mn^+ are oxidized to produce Ni^{2+}, Co^{2+}, and Mn^{2+} upon interaction with the metal cations anchored to the MXene-NF surface by the PO_4^{3-} ions [36].

$$Ni_{(3-x)}Co_{(x)}Mn_{(x)}(OH)_2 + 2HPO_4^{2-} \rightarrow Ni_{(3-x)}Co_{(x)}Mn_{(x)}(PO_4)_2 + 2H_2O \quad (7)$$

The random stacking formation of hybrid nanocrystalline particles of $Ni_{(3-x))}Co_{(x)}Mn_{(x)}(PO_4)_2$ on top of MXene-NF by the potentiodynamic electrodeposition approach at a potential of −1.0 V is confirmed by this reaction Eq. (7).

3.2. Structural and morphological characterization

The structural crystallinity and phase purity of the as-synthesized NCMP series and pristine MXene materials were examined using X-ray diffraction (XRD), as shown in Fig. 1(a). All samples (except the pristine MXene sample) exhibit poor crystallinity and show no obvious crystal diffraction peaks instead of NF peaks (denoted by the symbol (∗)), due to the existence of ultrathin nanostructures. However, the XRD pattern of the pristine MXene ($Ti_3C_2T_x$) sample reveals characteristic peaks of (0 0 2), (0 0 4), (0 0 6), (1 1 1), (1 0 3), (2 0 0), (2 2 0) planes corresponding to the peak positions at 8.98°, 19.78°, 29.92°, 35.12°, 37.84°, 41.70°, and 60.69°, respectively, and it clearly shows that MXene is cubic crystalline nature (JCPDS Card No.: 00-032-1383) (magnified image of XRD Fig. 1(b)) [37,38]. Meanwhile, the NCMP-5 sample exhibits a few weak diffraction peaks associated with MXene, confirming that the developed material is a composite of MXene with Ni-Co-Mn phosphate. Even so, the distinctive peak at 8.98° ascribed to the MXene nanosheets entirely vanished after the in-situ development of Ni-Co-Mn phosphate on MXene. This might be owing to the development of a thin layer of Ni-Co-Mn phosphate on both sides of the MXene nanosheets. On the other hand, the non-existence of a diffraction signal from the NCMP series electrode suggests the formation of the amorphous nature of Ni-Co-Mn phosphate material. Interestingly, the unevenly organized structure of the amorphous phase of material can offer enormous active sites and prolonged pseudocapacitive capacity, which can lead to better electrochemical activities compared to crystalline materials [9]. Additionally, an amorphous material structure might effectively sustain the swelling and diffusion of the electrolytic ions to improve durability than its crystalline counterparts [39].

To comprehend the vibrational modes of developed materials, the Raman analysis of pristine MXene, nickel (NCMP-1), cobalt (NCMP-2), manganese (NCMP-3), composites of Ni-Co-Mn phosphate (NCMP-4), and Ni-Co-Mn phosphate@MXene (NCMP-5) were performed and can be seen in Fig. 1(c). A Raman study of the NCMP series electrodes displays typical peaks in the 200–800 cm^{-1} range associated with metal-oxygen (M-O) vibration

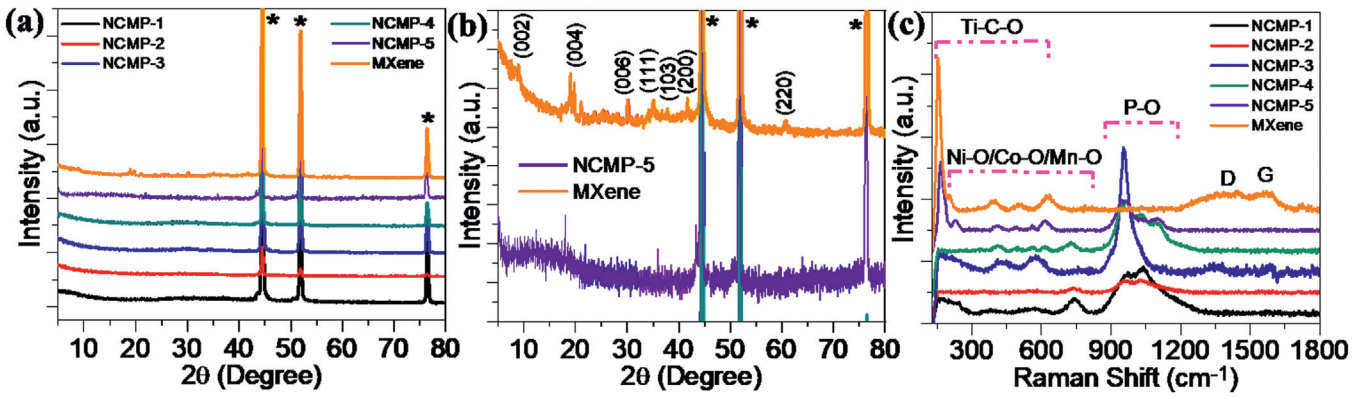

Fig. 1. (a, b) X-ray diffraction patterns, and (c) Raman spectra of MXene and NCMP series thin films.

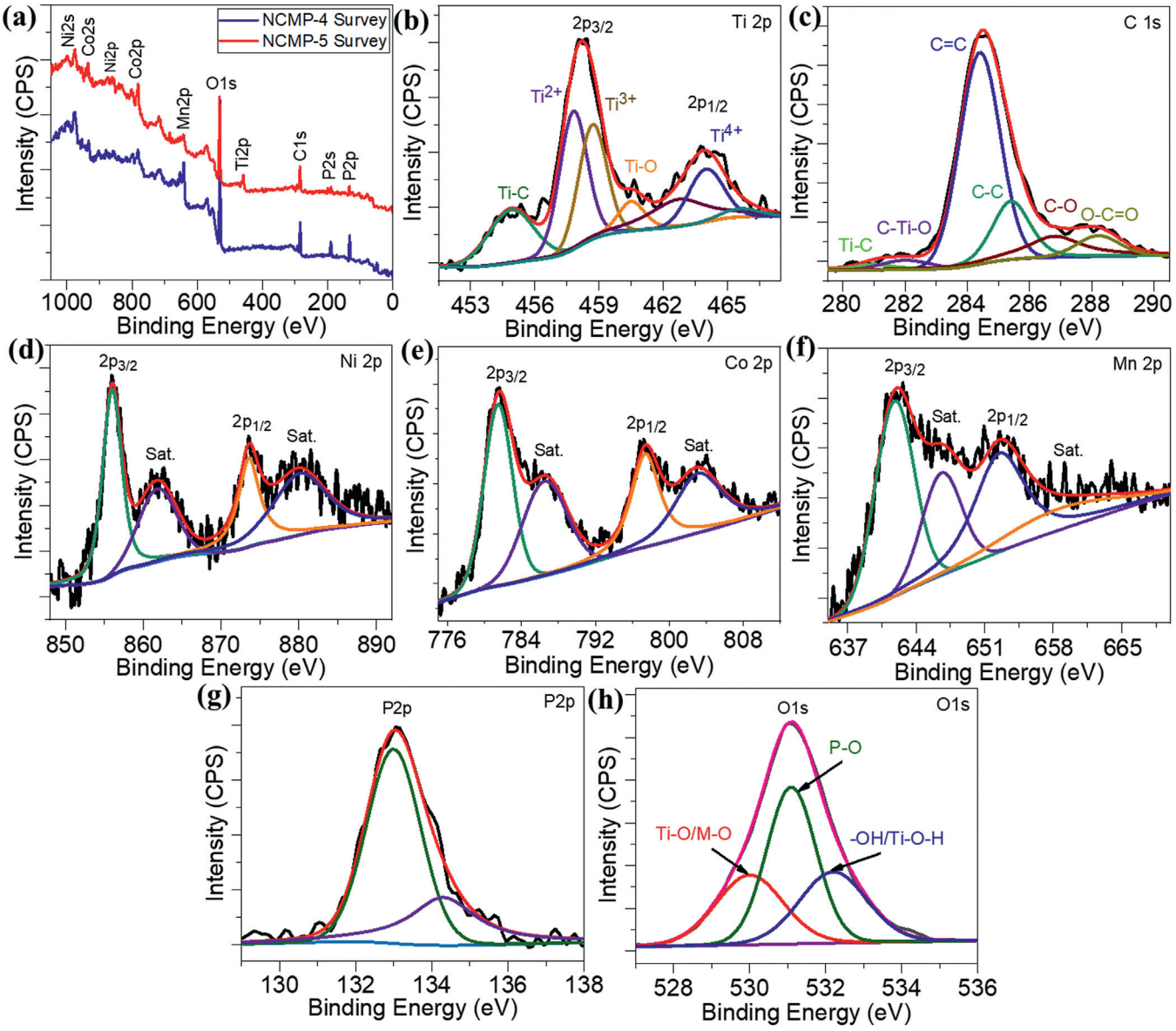

Fig. 2. (a) The XPS survey spectra of NCMP-4 and NCMP-5 electrodes, (b) Ti 2p, (c) C 1s, (d) Ni 2p, (e) Co 2p, (f) Mn 2p, (g) P 2p and (h) O 1s spectra of NCMP-5 thin film.

banding and the 900–1100 cm^{-1} range corresponding to phosphate banding. Specifically, Raman analysis revealed distinct vibration mode peaks for the pristine nickel phosphate sample at about 383, 570, and 743 cm^{-1}, which match the stretching vibrational mode of Ni–O and O–Ni–O [8,40,41]. Also, the peaks observed at 350, 493, 559, 615, and 737 cm^{-1} have been assigned to the stretching vibration of the O–Co–O and Co–O modes [42,43]. Likewise, the peaks at 406, 428, and 577 cm^{-1} are associated with the Mn–O stretching vibration band or bending of the Mn–O–Mn mode [8,44]. Furthermore, prominent peaks on the Raman spectra at 959, 970, 1029, 1040, and 1101 cm^{-1} are ascribed to the symmetric and antisymmetric stretching and vibrational modes of the P–O–P and PO_4^{3-} group, indicating the existence of phosphate into electrode materials [40,45]. However, the pristine and mixed Ni/Co/Mn phosphate (NCMP) (with MXene) samples revealed some analogous Raman vibration bands of Ni–Co–Mn–O, P–O, and Ti–C are shown in Fig. 1(c) [8,40]. In addition, the distinct peaks located at 154, 205, 396, 505, and 628 cm^{-1} were attributed to the Ti–C in-plane vibration and are shown in NCMP-5 and pristine MXene samples [46–48]. The Raman peaks of $Ti_3C_2T_x$ at 628 cm^{-1} and 396 cm^{-1} are assigned to the in-plane vibrations of the C and O atoms, respectively [49]. Furthermore, two peaks were detected at 1397 and 1570 cm^{-1}, associated with the disordered D-band and graphite G-band, respectively [46,50]. As a result, the NCMP series Raman spectra can be categorized as pristine and Ni-Co-Mn phosphate, indicating the successful synthesis of NCMP series materials and the presence of MXene in NCMP-5 thin film (except for the pristine MXene sample).

Furthermore, an X-ray photoelectron spectroscopy (XPS) study was used to identify the oxidation states and chemical composition of elements in the developed Ni-Co-Mn phosphate@MXene (NCMP-5) nanocomposite electrode (Fig. 2(a–h)). In this study, survey spectra of the NCMP-5 sample confirmed the occurrence of Ni, Co, Mn, P, O, Ti, and C elements in the material (Fig. 2(a)). In detail, the high-resolution Ti 2p XPS spectra (Fig. 2(b)) have been deconvoluted into five binding energies at 454.7, 457.5, 458.5, 460.2, and 464.1 eV, which may be originated from Ti-C, Ti^{2+}, Ti^{3+}, Ti-O, and Ti^{4+}, respectively, and are in good accord with previous XPS investigations [51]. Fig. 2(c) shows a deconvoluted C 1s spectra with six distinctive peaks at 281.1, 282.0, 284.3, 285.0, 286.5, and 288.0 eV,

which are assigned to Ti-C, C-Ti=O, C=C, C-C, C-O, and O-C=O, respectively [52]. Fig. 2(d–f) illustrates the high-resolution Ni 2p, Co 2p, and Mn 2p XPS spectra fitted by employing the Gaussian strategy. For all these spectra, two spin-orbit doublets with two shake-up satellites (designated as "Sat.") provide the best fit. Particularly, two prominent peaks of Ni 2p spectra detected at 856.0 and 873.6 eV binding energies define the Ni $2p_{3/2}$ and Ni $2p_{1/2}$ states, corresponding to the oxidation state of Ni^{2+} (Fig. 2(d)) [53]. The two strong peaks in the Co 2p spectra at 781.5 eV in Co $2p_{3/2}$ and 797.4 eV in Co $2p_{1/2}$ are ascribed to the Co^{2+} oxidation state (Fig. 2(e)) [10]. In addition, two strong peaks in the Mn 2p core-level spectra (Fig. 2(f)) at 641.9 and 652.7 eV are attributed to Mn $2p_{3/2}$ and Mn $2p_{1/2}$, respectively, indicating the oxidation state of Mn^{2+} [53]. According to this XPS investigation, every transition metal element is divalent, which promotes the amorphous Ni-Co-Mn phosphate formation. Following that, the XPS spectra of P 2p (as shown in Fig. 2(g)) revealed two fitting peaks: one at 134.3 eV belonged to the phosphate (PO_4^{3-}) group [54] and the other at 133.0 eV for the P-O bond [53]. These observed peaks suggested the existence of phosphate species in the NCMP electrode materials. Also, the analysis of the O 1s XPS spectra (Fig. 2(h)) indicated that the metal-oxide (M-O) or Ti-O fitting peak was located at 530.0 eV [55,56], and the phosphorus-oxygen (P-O) bond and chemically or physically adsorbed water or moisture (-OH)/Ti-O-H molecules were 531.1 and 532.2 eV, respectively [9,56]. Thus, the XPS results reveal the effective synthesis of Ni-Co-Mn phosphate material on MXene nanosheets using a simple electrodeposition approach. Most notably, the lattice sites are contributed by cations of Ni, Co, and Mn which have quite comparable oxidation states [57].

Following that, the detailed structural characteristics of the NCMP series and pristine MXene samples were analyzed by FE-SEM (Hitachi, SU8600) at the Smart Materials Research Center for IoT at Gachon University. In this investigation, Figs. 3(a-f) and S1(a–f) illustrate FE-SEM images of the NCMP series and pristine MXene samples at various magnifications (500X, 9kX, and 100kX). Subsequently, Fig. S1(a–f) displays low-magnification (500X) pictures of all as-synthesized samples (including the MXene sample), revealing that the NF framework is completely covered (high-density growth) by synthesized material with the nano/microarchitecture following electrodeposition growth. However, it is interesting to note that during film development, the Ni:Co:Mn atomic concentration ratio affects the formation of nano/microstructure. Because the ionic radii of nickel (83 pm) for Ni^{2+}, manganese (81 pm) for Mn^{2+}, and cobalt (79 pm) for the Co^{2+} oxidation state are different. Furthermore, to maintain the charge neutrality of $(PO_4)^{3-}$, there are possible rearrangements in the ionic concentrations of $Ni^{2+}/Co^{2+}/Mn^{2+}$, which might cause morphological alterations. To begin, as can be seen from the high-resolution FE-SEM image in Fig. 3(a, b), pristine nickel (NCMP-1) and cobalt phosphate (NCMP-2) are composed of numerous irregularly shaped, porous, and interconnected NPs on the NF surface, with sizes ranging from around 250 nm to 1.3 µm. Fig. 3(c) shows vertically aligned nano/micro flowers with flake-like structures in pristine manganese phosphate (NCMP-3). These interconnected nano/micro flakes are closely stacked, and the size of the flakes is between 500 nm to 1.5 µm. In addition, the FE-SEM illustration of Ni-Co-Mn ternary phosphate (NCMP-4) in Fig. 3(d) displays a particle-like structure that clumps together to form a larger agglomerated hierarchical porous microstructure (or caterpillar-type surface) and having a particle size ranging from 1 to 4 µm. This might be due to the synergistic coalescence process of Ni-Co-Mn in the NCMP-4 sample and the protrusion of the unique manganese phosphate nanoflowers. Fig. 3(e) shows the FE-SEM image of Ni-Co-Mn phosphate@MXene (NCMP-5) nanocomposite structure, in which Ni-Co-Mn phosphate was electrodeposited on MXene coated NF surface in the electrolyte solution. This picture also illustrates the insertion of Ni-Co-Mn phosphate particles in the intermediate and on the surface layers of the MXene matrix frameworks, implying that the NCMP has been effectively constructed on the MXene surface. More closely, the FE-SEM analysis shows that the deposition produces interconnected, well-dispersed 3D porous NPs on 2D nanosheets (inset Fig. 3(e)). The estimated thickness of a single nanosheet is 30–55 nm, whereas the thickness of particles is also 600 nm to 2.2 µm. This Ni-Co-Mn phosphate@MXene nanocomposite may provide shorter ion diffusion pathways, richer redox active sites, and increased surface area, which could improve interlayer structural stability, reaction kinetics, and specific capacity [14,26]. Besides, the pristine MXene sample (Fig. 3(f)) showed a 2D thin nanosheet-like structure with a smooth surface and thickness of around 25 to 45 nm in the inset of Fig. 3(f). These 2D nanosheets are interconnected and provide a high surface area and an abundance of intricate holes for NCMP material, facilitating efficient charge transfer and increasing the number of electro-active sites while also accelerating electrolyte penetration [58]. In addition, with the assistance of high-resolution (HR) transmission electron microscopy (TEM), the morphology of the NCMP-5 nanocomposite is further investigated (Fig. 3(g, h)). As observed in the TEM images, the MXene nanosheets have a dark background (specifically at the edges) and NCMP NPs are irregularly evident on the surface of MXene sheets, indicating the ultrathin nature of the nanosheets and confirmed to be Ni-Co-Mn phosphate. Therefore, a high specific capacity might be anticipated through the complete utilization of active materials and a lot of surface exposure. Interestingly, no Ni-Co-Mn phosphate material has been identified, whereas only the MXene lattice fringe is observed even in the HR-TEM picture (Fig. 3(h)), indicating that those NPs are in an amorphous phase.

Afterward, energy dispersive X-ray spectroscopy (EDX) was utilized for assessing the elemental analysis and purity of the as-synthesized NCMP and MXene materials (Fig. S2(a–f)). The Ni, Co, Mn, P, O, Ti, and C elements exhibit prominent peaks in the EDX spectrum, and each element has been observed in the corresponding samples. The EDX spectrum shows no additional impurity peaks, indicating that the resultant materials are uncontaminated. Furthermore, both observed and experimental Ni:Co:Mn and Ni:Co:Mn:P atomic ratios are almost similar for all synthesized thin films. The stoichiometric ratios and proportions of existing elements in all synthesized thin films are indicated in Table S1. For further study of the element composition, elemental mapping analysis was carried out on the NCMP-5 sample, which was manufactured under optimal conditions. Fig. S3(a–h) depicts the entire elemental mapping, highlighting the specific elements including Ni, Co, Mn, P, O, Ti, and C. The mapping pictures demonstrated the homogeneous distribution of every element over the electrodeposited NCMP-5 sample.

3.3. Electrochemical behavior of NCMP electrodes

Generally, the highest integral at an equimolar amount of all metals implies that the maximal synergistic impact between each metal occurs when they are present in equivalent proportions in the electrodeposition solution [14]. Therefore, to probe the electrochemical features of the as-synthesized NCMP and pristine MXene electrodes, electrochemical experiments were conducted in a three-electrode system with an aqueous 1 M KOH electrolyte. Initially, the cyclic voltammetry (CV) curves of the NCMP electrodes are tested at a 50 mV/s sweep rate with the potential ranging from 0.0 to 0.7 V/Hg/HgO, as shown in Fig. 4(a). According to the CV profile (Fig. 4(a)), the NCMP-5 achieved the optimum electrochemical property after 10 min of electrodeposition synthesis

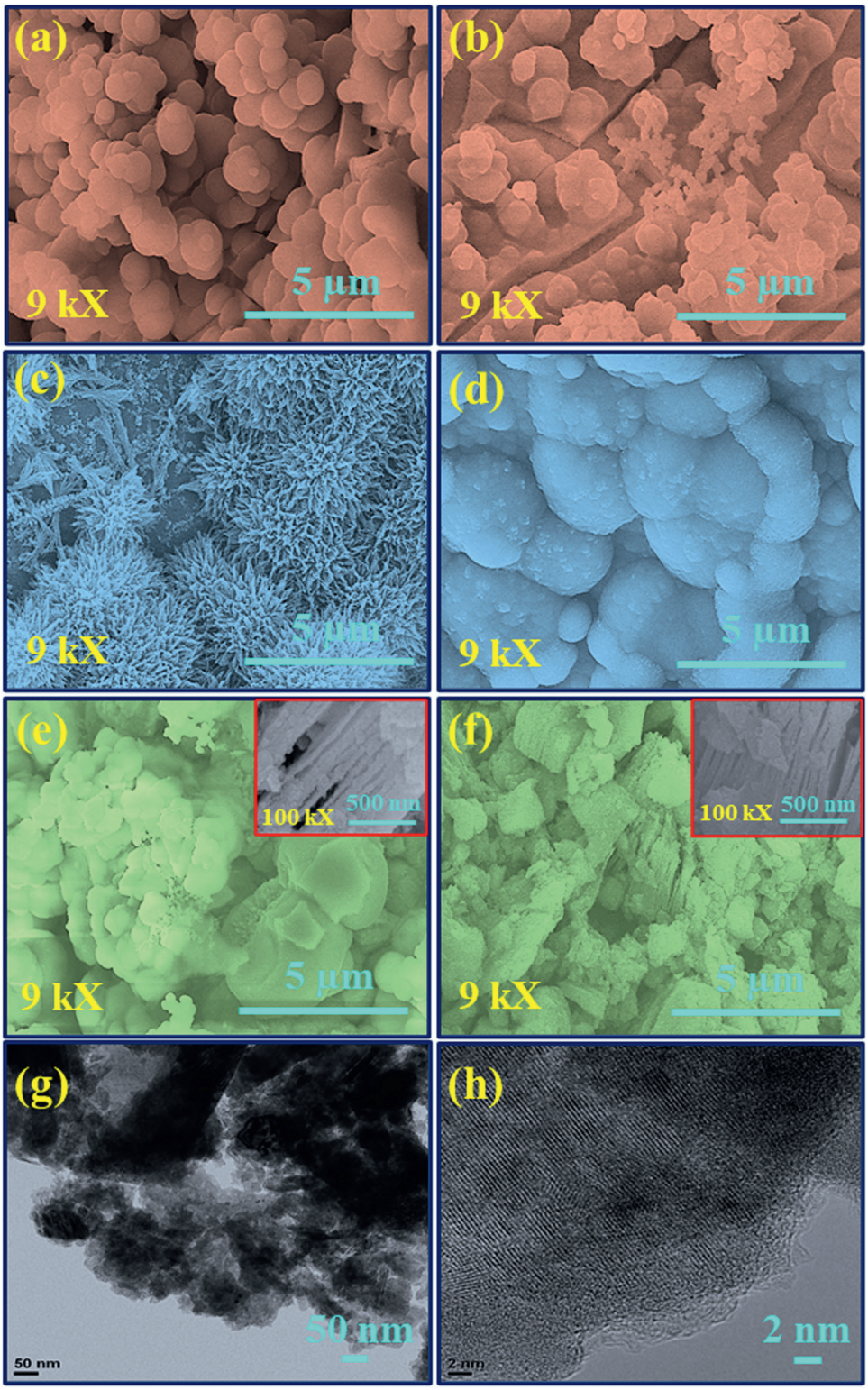

Fig. 3. FE-SEM of (a) NCMP-1, (b) NCMP-2, (c) NCMP-3, (d) NCMP-4 (e) NCMP-5, (f) MXene thin films at 9kX magnifications, and (g) HR-TEM image of NCMP-5 (h) with the distance between the lattice planes of MXene.

by attaining the highest current density and current area under the curve. Also, the NCMP-5 sample exhibited significantly faster redox kinetics and high electrical conductivity due to the NCMP NPs anchored on the conductive $Ti_3C_2T_x$ nanosheet support, which might be attributed to the quick electron transfer between Ni-Co-Mn phosphate to MXene [59]. In addition, layered MXene structure offers additional active sites that allow electrolyte ions to deeply penetrate the MXene interlayer gap and their 2D structure along with metallic conductive properties facilitates the rapid movement of charge carriers (ions or electrons) within the material [60]. Fig. 4(a) compares the efficiency of the ternary phosphate electrode with those of single phosphates, indicating the advantages of integrating three metals into a single electrode. Furthermore, the CV curves of NCMP-5 were analyzed at scanning rates

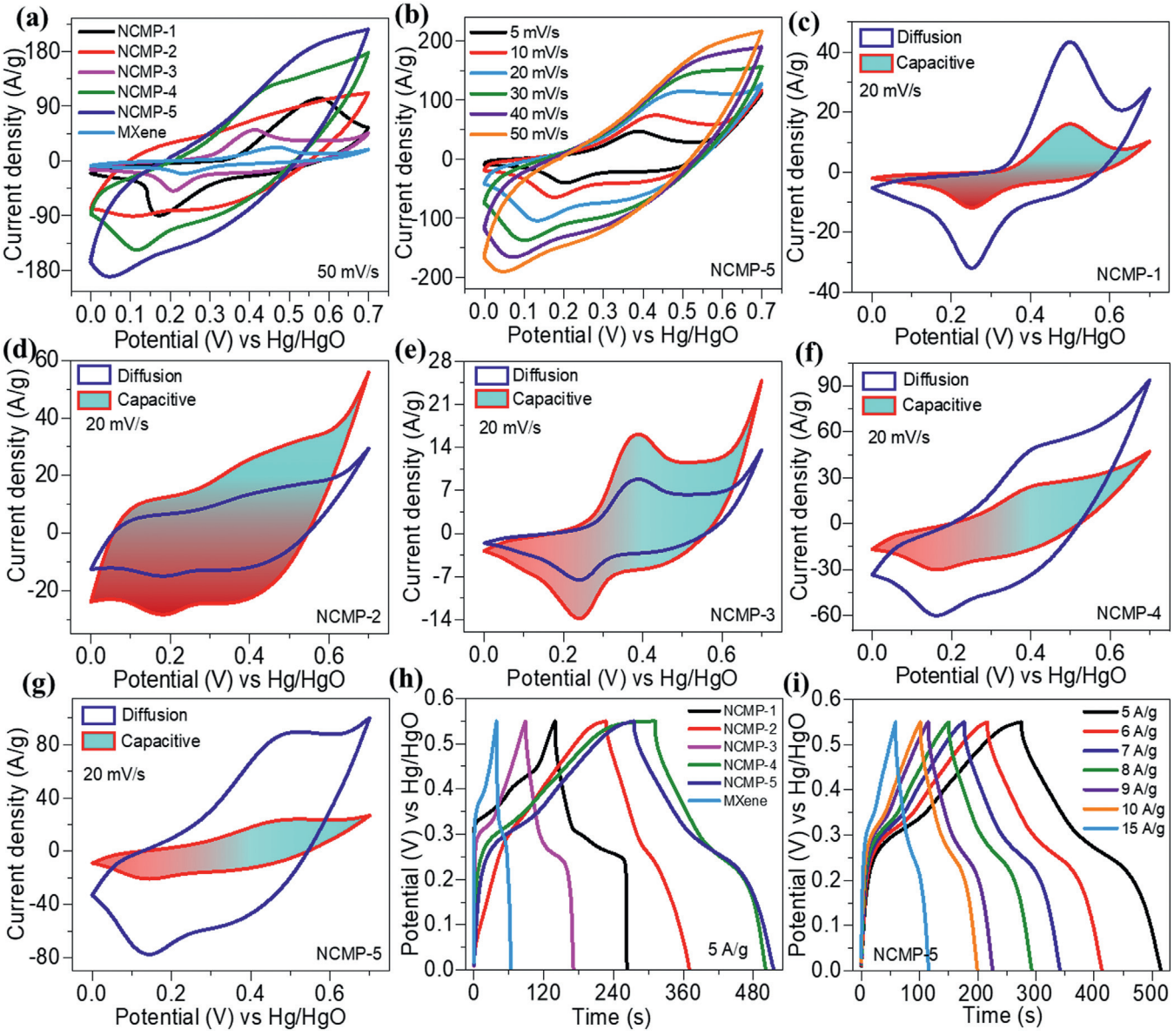

Fig. 4. (a) CV plots of NCMP series thin films at a fixed sweep rate of 50 mV/s, (b) CV plots of NCMP-5 electrode at different sweep rates of 5–50 mV/s, (c–g) CV curves with the capacitive and diffusion-controlled currents for the NCMP series thin films at 20 mV/s sweep rate, (h) GCD plots of NCMP series thin films at 5 A/g fixed current density, and (i) GCD plots of NCMP-5 electrode at various current densities of 5–15 A/g.

ranging from 5 to 50 mV/s (Fig. 4(b)), and the results revealed that the shapes were similar, and the redox peaks corresponded to the M^{2+} reaction (where M is Ni, Co, or Mn). Similarly, Fig. S4(a–e) depicts the remaining CV curves of NCMP series electrodes at a sweep rate ranging from 5 to 50 mV/s. All CV redox peaks shifted toward higher and lower potentials as the sweep rate increased, indicating strong conductivity and fast ion transport kinetics. Moreover, the existence of obvious redox peaks on each CV curve caused by the Faraday reaction between $Ni/Co/Mn(PO_4)_2$, $NiCoMn(PO_4)_2$, and OH^- ions, symbolizes a characteristic of battery-type supercapacitor electrode materials [61]. The following reversible equation describes the reaction mechanism:

$$Ni_{(3-x)}Co_{(x)}Mn_{(x)}(PO_4)_2 + OH^- \rightarrow Ni_{(3-x)}Co_{(x)}Mn_{(x)}(PO_4)_2(OH) + e^- \quad (8)$$

Nonetheless, nickel is a transitional metal with faradaic battery-like activity, whereas manganese and cobalt highlight capacitance through an inherent pseudocapacitive-type mechanism [14]. Consequently, all three metals have an enormous impact on the entire electrochemical efficiency as the ternary composition acquires the benefits from each of its single phosphate substitutes, including rich manganese redox chemistry, the excellent capacity of nickel, and the high stability of cobalt/manganese [14]. According to morphological characteristics investigations of NCMP-5 materials, the NPs anchored on the nanosheet surface, boosting its specific surface area, and electroactive sites than other NCMP materials, thereby offering higher electrochemical efficiency.

Besides, the electrochemical reaction process of the synthesized thin film was investigated using CV plots by Eq. (9), which depends on the relation between sweep rate (v) and current density (i) [16].

$$i = av^b \quad (9)$$

Where both a and b are constant coefficients, however, the b value is derived from the slope of log (i) vs. log (v). Generally, the electrochemical mechanism of the electrode is surface-controlled when the value of b is near 1 and diffusion-controlled when it is close to

Table 2
Comparative literature survey for the capacitive performance of Ni-Co-Mn-based electrodes.

Sr. No.	Material and structure	Substrate	Method of deposition	Electrolyte	Specific capacitance & current density	Cycles (Stability)	Refs.
1.	$Ni_2Co_{0.75}Mn_{0.25}$-MOFs-S (Cuboid Nanorods)	NF	HD	3 M KOH	1428 F/g at 1.0 A/g	3000 (83.5 %)	[2]
2.	Ni-Co-Mo phosphide (Nanoarrays)	CC	HD/Ph	6 M KOH	508 F/g at 0.2 A/g	–	[7]
3.	Fe-Co-Ni phosphide (Nanosheet Arrays)	CC	ED/ PECVD	2 M KOH	593.0 C/g at 1.0 A/g	5000 (84.2 %)	[13]
4.	Mn-Ni-Co phosphide (Flower)	NF	ED/ PECVD	1 M KOH	1690 C/g at 1.0 A/g	850 (97 %)	[14]
5.	Zn-Ni-Co phosphide (Nanowire Arrays)	NF	HD/Ph	3 M KOH	1269 C/g at 3.0 A/g	–	[15]
6.	NiCoMn-LDH@PPy-C (3D Flower)	NF	HD/CVD	1 M KOH	3157.78 F/g at 1.0 A/g	10,000 (90.5 %)	[31]
7.	NiCoMn phosphide (Nanosheets)	NF	HD/Ph	1 M KOH	1063 C/g at 1.0 A/g	–	[65]
8.	$Zn_{0.50}Co_{0.50}Mn(PO_4)_2$ (Nanoflake)	NF	SC	1 M KOH	1022.52 C/g at 1.2 A/g	–	[66]
9.	Ni-Co-Mn sulfide (Neuron-like)	NF	HD	2 M KOH	2805.3 F/g at 1.0 A/g	10,000 (82.9 %)	[67]
10.	Ni-Co-Mn-OH (Nanosheets)	CC	HD	3 M KOH	2070 F/g at 1.0 A/g	10,000 (92.2 %)	[68]
11.	NiCoMn-O (Prism-like)	NF	CP	3 M KOH	1623.5 F/g at 1.0 A/g	5000 (97.7 %)	[69]
12.	Ni-Co-Mn phosphate@ MXene (Nanoparticles/ Sheets)	NF	ED	1 M KOH	1230 C/g (342 mAh/g) at 5.0 A/g	5000 (98.8 %)	Our work

Note: NF—Nickel Foam, CC—Carbon Cloth, ED—Electrodeposition, Ph—Phosphorization, CP—Co-Precipitation, SC—Sonochemical, CBD-C—Chemical Bath Deposition-Calcination, HD—Hydrothermal, PECVD— Plasma Enhanced Chemical Vapor Deposition.

0.5 [9]. Based on the assumptions stated above, the anodic peaks of the NCMP-1, NCMP-2, NCMP-3, NCMP-4, and NCMP-5 electrodes are represented by the values of b in Fig. S5(a–e), which are 0.57, 0.69, 0.66, 0.63, and 0.60, respectively. It implies that diffusion-controlled behavior dominates in the charge storage mechanism of the NCMP-1, NCMP-4, and NCMP-5 electrodes, which is related to the properties of material like the battery-type [16]. However, the surface-controlled response dominates the electrochemical reaction of NCMP-2 and NCMP-3 electrodes.

Moreover, the contributions of the diffusion- and surface-controlled processes were assessed using Eqs. (10) and (11) [13]:

$$i = i_{cap} + i_{diff} = k_1 v + k_2 v^{\frac{1}{2}} \tag{10}$$

$$\frac{i(V)}{v^{\frac{1}{2}}} = k_1 v^{\frac{1}{2}} + k_2 v \tag{11}$$

Where $k_1 v$ and $k_2 v^{1/2}$ denote the capacitive and diffusion-controlled contributions, respectively, i and v denote the current at a given voltage and sweep rate. As shown in Fig. 4(c–g), diffusion-controlled contributions contribute to 72.94 %, 34.49 %, 35.37 %, 66.58 %, and 78.87 % of the entire capacity at 20 mV/s for NCMP-1, NCMP-2, NCMP-3, NCMP-4, and NCMP-5 electrodes, respectively. The contribution percentage ratios of all thin films are described in Fig. S6(a–e). Further, the contributions of the diffusion-controlled process for all electrodes steadily decreased to 63.03 %, 24.98 %, 25.71 %, 55.75 %, and 70.24 %, respectively, as the scan rate amplified to 50 mV/s, caused by inadequate diffusion period from ions to latices during elevated sweep rates [62]. Meanwhile, all electrodes exhibit fast charge and ion diffusion in the improved capacitive-controlled contribution with increasing sweep rate, which can be attributed to their well-constructed nanostructures, and an abundance of redox-active sites [13].

Likewise, the galvanostatic charge-discharge (GCD) assessment was exploited to explore the storage properties of pristine MXene and NCMP-series electrodes at 5 A/g in the voltage range of 0.0 to 0.55 V/Hg/HgO, as demonstrated in Fig. 4(h). According to this investigation, the NCMP-5 electrode has a longer discharge time than the other NCMP electrodes, proving that the insertion of MXene has significantly increased its maximum specific capacity. Its improved energy storage capacity might be due to its hierarchical nanostructures, which deliver efficient ion transfer networks and electrochemically active sites [63]. To better confirm the charge storage capacity and rate efficiency, the GCD profiles of NCMP-1, NCMP-2, NCMP-3, NCMP-4, NCMP-5, and MXene electrodes under different applied currents of 5–15 A/g are shown in Figs. 4(i) and S7(a–e). These results revealed that all electrodes displayed typical quasi-triangular (non-linear) GCD curves due to a combination of electric double-layer capacitive (EDLC) and pseudocapacitive characteristics, suggesting their excellent chemical reversibility [18]. Also, the well-defined voltage plateau reveals that the electrodes exhibit a Faraday redox approach, and the remarkably symmetrical charge/discharge properties imply a rapid I–V response [64]. Every voltage platform corresponds to the oxidation/reduction peak of the CV as previously described in Fig. 4(a), demonstrating that the NCMP-5 dominated battery-type charge storage activities (Fig. 4(g)). Meanwhile, Fig. 5(a) depicts the specific capacity plot of the NCMP series electrode, which was calculated using equations S2 and S4. The specific capacity of NCMP-1, NCMP-2, NCMP-3, NCMP-4, NCMP-5, and MXene electrodes reaches 174 mAh/g (629 C/g), 198 mAh/g (715 C/g), 113 mAh/g (409 C/g), 259 mAh/g (935 C/g), 342 mAh/g (1230 C/g), and 33 mAh/g (119 C/g) at 5.0 A/g, respectively. The NCMP-5 electrode retains 76 % of its initial specific capacity at 5 A/g when the current density rises to 15 A/g. This is significantly larger than the NCMP-4 electrode, which has a capacity retention rate of 74 % and is comparable to the previous electrode materials with an equivalent structure, as listed in Table 2 [2,7,13-15,31,65-69]. In comparison with the other samples, the NCMP-5 electrode exhibited the highest specific capacity and optimal rate performance. This outcome was achieved by the unique combination of Ni, Co, and Mn active species, as well as its hierarchical porous nanosheets with nanoparticle-like structure, quick ion/electron transport channels, and an abundance of exposed redox active sites [13]. Additionally, the high electrical conductivity of MXene as a 2D layered material significantly boosted the efficiency of the NCMP-5 electrode. Also, this MXene not only contributed to a wider attachment area but also provided a better alkali metal cation adsorption capacity [70]. As a result, the inclusion of MXene effectively enhanced the electrochemical efficiency of the NCMP-5 electrode.

Thereafter, electrochemical impedance spectroscopy (EIS) studies were performed on the NCMP electrode materials to investigate the properties of efficient electron transportation and quick ion diffusion during the Faraday reaction. The Nyquist diagrams of the NCMP series electrodes are presented in Fig. 5(b) and its magnified image as well as the fitted equivalent circuit of the NCMP-5 sample, is shown in the inset of Fig. 5(b). In the present investigation, the equivalent series resistance (R_S) of an electrode is represented by the intercept on the real axis of the curve, which reflects

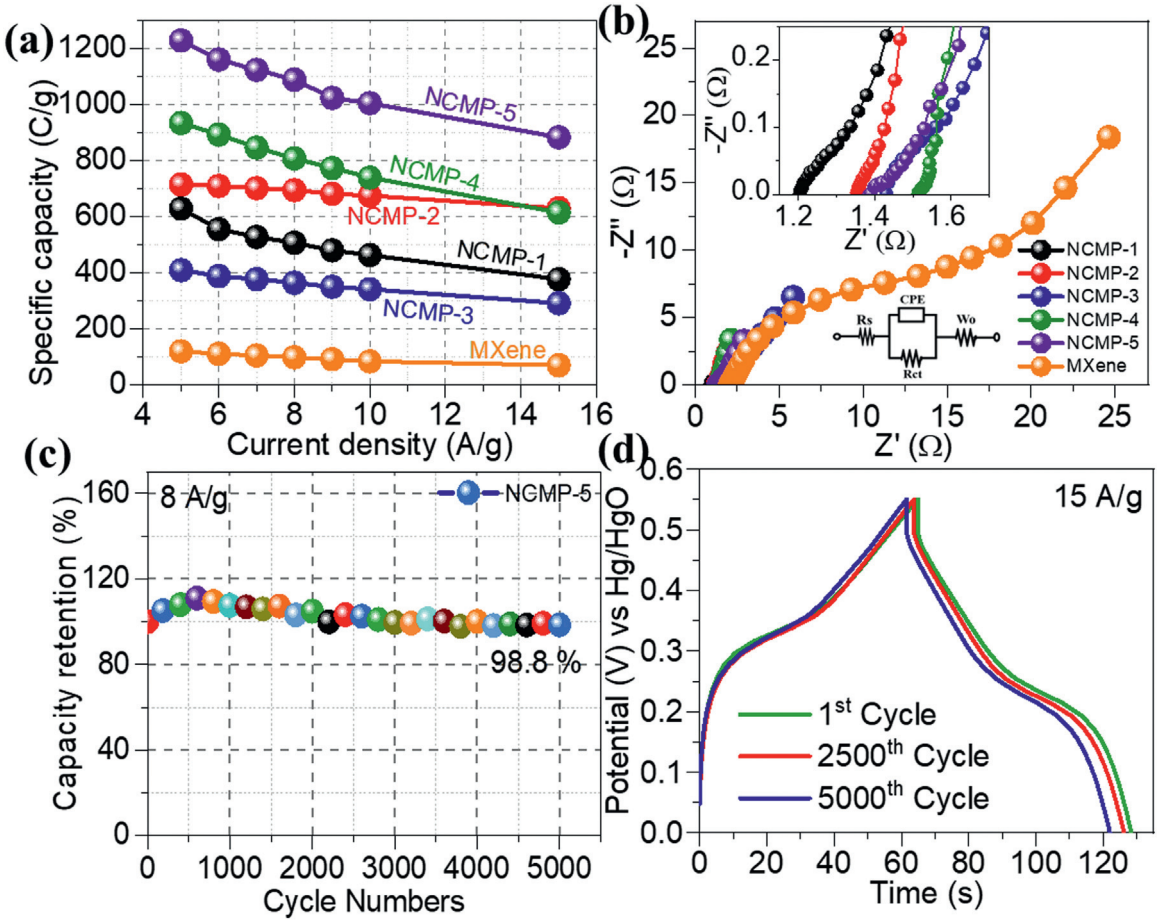

Fig. 5. (a) Graph of specific capacity vs. current density, (b) Nyquist plots of NCMP series electrodes [Inset: (i) magnified Nyquist plots (ii) fitted equivalent circuit of NCMP-5], (c) stability graph for 5000 cycles, and (d) 1st, 2500th and 5000th GCD cycles of NCMP-5 electrode.

the contact resistance of the system and the intrinsic resistance of active material [63]. In addition, the semi-circular arc symbolizes the charge transfer resistance (R_{ct}) or Faradic resistance between the electrolyte and electrode, as well as the constant phase elements (CPE) indicate the EDLC mechanism. Also, the straight slope mostly corresponds to the ion transmitting resistance (W_o, Warburg element) during the diffusion process resistance to investigate the electrolyte diffusion within the electrode. Fig. 5(b) shows that NCMP-5 (0.25 Ω) has the lowest R_{ct} when compared to NCMP-1 (0.32 Ω), NCMP-2 (0.40 Ω), NCMP-3 (0.55 Ω), NCMP-4 (0.29 Ω), and MXene (25.7 Ω) electrodes. According to the graph analysis, NCMP-5 has a significant straight-line slope and the lowest semicircle diameter among the other samples, suggesting that it has a quicker electron transport mechanism and the lowest ion diffusion resistance of electrolytes. Additionally, smaller R_S and R_{ct} values showed an expanded electroactive area and the higher conductivity of MXene increased the electrical conductivity of the NCMP-5 electrode material [71]. To be conclusive, the 3D Ni-Co-Mn phosphate provides plenty of electroactive sites and improves the penetrability of the electrolyte characteristics, and the 2D layered structure of MXene provides a suitable pathway for free ion transport in the electroactive materials. As a result, the NCMP-5 electrode has the lowest total resistance.

Moreover, the cycle life is a crucial factor in assessing the characteristics of hybrid energy storage. In this study, the cycle stability of the NCMP-5 electrode was estimated using GCD tests at 15 A/g current density, as shown in Fig. 5(c). After 5000 GCD cycles, this electrode shows notable cyclic stability, retaining 98.8 % of its initial capacity. Fig. 5(d) also shows the GCD plots at the 1st, 2500th, and 5000th cycles of the NCMP-5 electrode. The key factor that contributed to this excellent stability is stable nanostructures, which provide efficient electron transmission and ion adsorption/desorption. In this study, it is noteworthy that it has a small boost in specific capacity at the initial phase of the cycle, which might be explained by the electrolyte penetrating more deeply due to the redox reaction between the Ni-Co-Mn phosphate and MXene active material, thereby increasing their contact area. Notwithstanding, this graph also implies that a minor proportion of the nanostructure was degraded, leading to a capacity reduction as the number of cycles increased. Besides, during the cycling, the volume of Ni-Co-Mn phosphate and MXene materials constricted and expanded, and the nanostructure exposed more active sites, making them suitable for fast electron and ion transport during the redox process [63]. This higher cycle stability of the NCMP-5 nanocomposite might be attributed to its enhanced electrical conductivity, porosity, large specific surface area, quick ion/electron transport/diffusion, and elevated structural stability [14]. Furthermore, the electrochemical properties of the electrode in the present research are compared with other similar electrodes that have previously been published as displayed in Table 2 [2,13,14,31,67-69].

Based on the aforementioned investigation, the Ni-Co-Mn phosphate@MXene (NCMP-5) electrode material exhibits excellent specific capacity, outstanding rate capability, and superb cyclability, which may be due to the following factors: [72] (a) initially, the NF was used as a conductive and binder-free current collector to minimize contact resistance and improve the integrity of the structure; (b) the unique 3D@2D nanoarchitecture helps to reduce vol-

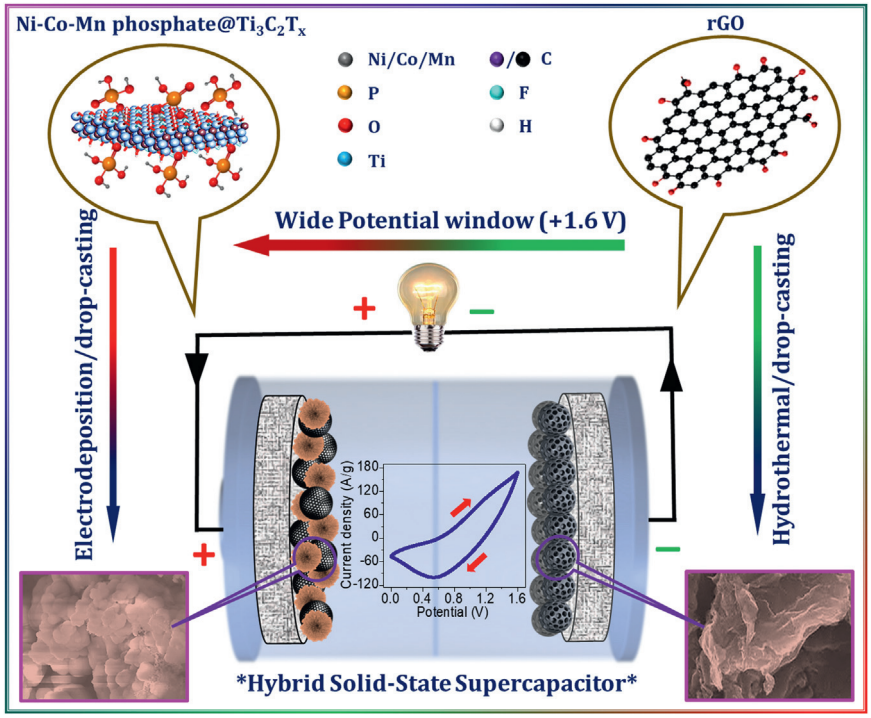

Scheme 2. Schematic illustration of the fabrication of NCMP-5//rGO hybrid solid-state supercapacitor (HSSC).

ume enlargement during the charge-discharge process and provides transportation channels for the movement of ions and electrons; (c) also, the abundant active sites are offered by the increased specific surface area, and the improved pore volume/size help to accelerate redox processes and fast electrolytic diffusion; (d) moreover, the synergistic effects of Ni-Co-Mn and Ti_3C_2 multimetals, lead to superior charge storage capability to get enhanced electrochemical efficiency.

3.4. Electrochemical study of Ni-Co-Mn Phosphate@mxene//rGO HSSC device

Nowadays, hybrid solid-state supercapacitors have gained a lot of interest owing to their high specific energy, superior cyclability, compact size, lightweight, and functional reliability [69]. Hence, to gain additional insight into the application of NCMP-5 thin film as a cathode material in a two-electrode system, an NCMP-5//rGO HSSC (rGO serving as the anode) device was successfully manufactured in PVA-KOH gel electrolyte, as presented diagrammatically in Scheme 2. Before fabricating the NCMP-5//rGO HSSC device in this research, a detailed evaluation (structural and electrochemical) of the rGO as a negative electrode material was presented in our previously published work [8].

Subsequently, the CV curves of the NCMP-5 and rGO were examined using a three-electrode configuration in a 1 M KOH electrolyte at a 50 mV/s sweep rate, as shown in Fig. 6(a). This figure highlights the battery-like characteristics of NCMP-5 and EDL-type charge storage behavior of rGO electrodes. Likewise, to identify the optimum operating voltage of the HSSC device, CV measurements were carried out at a 50 mV/s sweep rate within numerous potential regions ranging from 0.0 to 1.2 V to 0.0–1.7 V, as depicted in Fig. 6(b). However, if the voltage reaches +1.7 V, hydrogen/oxygen evolution occurs [14]. Therefore, it is determined that 0.0–1.6 V is the appropriate operational potential window for the HSSC device. Further, Fig. 6(c) illustrates the CV profiles of the HSSC device at numerous scanning rates ranging from 5 to 50 mV/s, which exhibit the synergistic benefits of the NCMP-5 and rGO electrodes for charge storage. These CV curves show almost rectangular symmetric CV profiles with weak redox peaks, indicating a Faradaic pseudocapacitive characteristic in the NCMP-5//rGO HSSC device, and smaller capacity degradation at various scanning rates suggests a quick ion transport mechanism and strong rate capability [73]. Even when the rate of scanning rises from 5 to 50 mV/s, the shapes of CV curves maintain substantially instead of any noticeable alteration, confirming its high reversible properties and quick charge-discharge efficiency [13].

Similarly, the GCD profiles recorded for different potentials (0.0–1.2 to 0.0–1.7 V) at 2 A/g current density, provide additional evidence of the utmost optimal voltage window of the NCMP-5//rGO HSSC device. Fig. 6(d) verifies that +1.6 V is the appropriate operating voltage for the NCMP-5//rGO HSSC device since a higher potential limit of +1.7 V displays twice of charging time as long as the discharge time. Also, the deformed GCD curve at +1.7 V suggests an oxygen evolution process or an irreversible phase change of surface groups [14]. For this reason, +1.7 V is considered as an unsafe potential for overcharging and inadequate device reversibility. Hence, to prevent polarization and instability during device operation, all measurements were performed in the voltage range of 0.0–1.6 V [74]. In this investigation, the GCD curves of the NCMP-5//rGO HSSC device were tested at different specific currents ranging from 1 to 6 A/g, which are depicted in Fig. 6(e). Moreover, the NCMP-5//rGO HSSC device exhibits semi-triangular and non-linear discharge behavior in these GCD curves, demonstrating its Faradaic pseudocapacitive nature and strong reversibility. The collective results confirm that the constructed NCMP-5//rGO HSSC device can function appropriately at a substantially higher operating potential of about +1.6 V due to the combined effect of operational voltage from individual electrodes. Therefore, to verify whether the device functions efficiently, the specific capacity of the device is computed at different current densities using the discharge curves depending on the combined weight of both (NCMP-5 and rGO) active materials and displayed in Fig. 7(a). The device delivers an elevated specific capacity of approximately 27.5 mAh/g (99 C/g) at a current density of 1 A/g, while it remains at 20.8 mAh/g (75

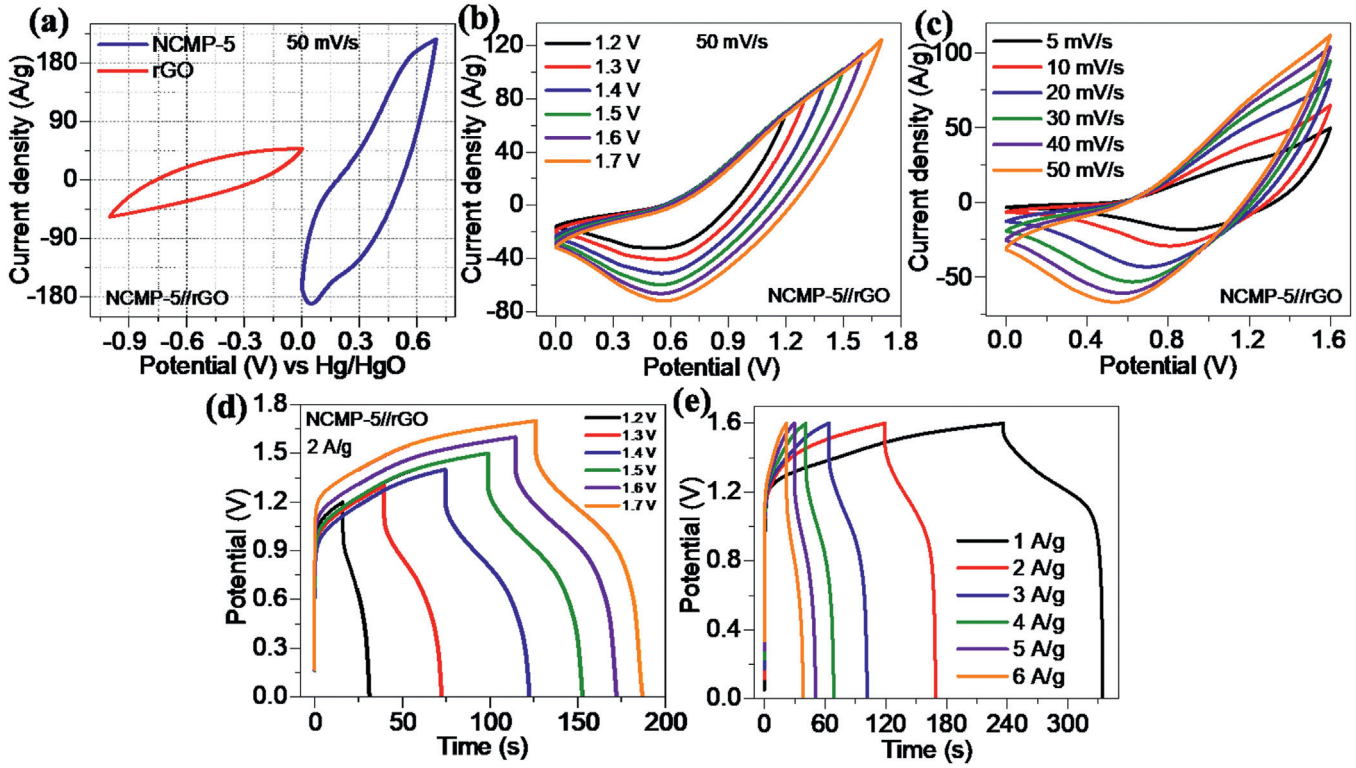

Fig. 6. (a) CV plots of NCMP-5 and rGO electrodes at 50 mV/s scan rate, (b) CV plots at diverse voltage windows from +1.2 to +1.7 V at 50 mV/s, and (c) at various sweep rates (5–50 mV/s), (d) GCD plots at various operating voltage windows from +1.2 to +1.7 V at 2 A/g, and (e) at 1–6 A/g current densities of HSSC device.

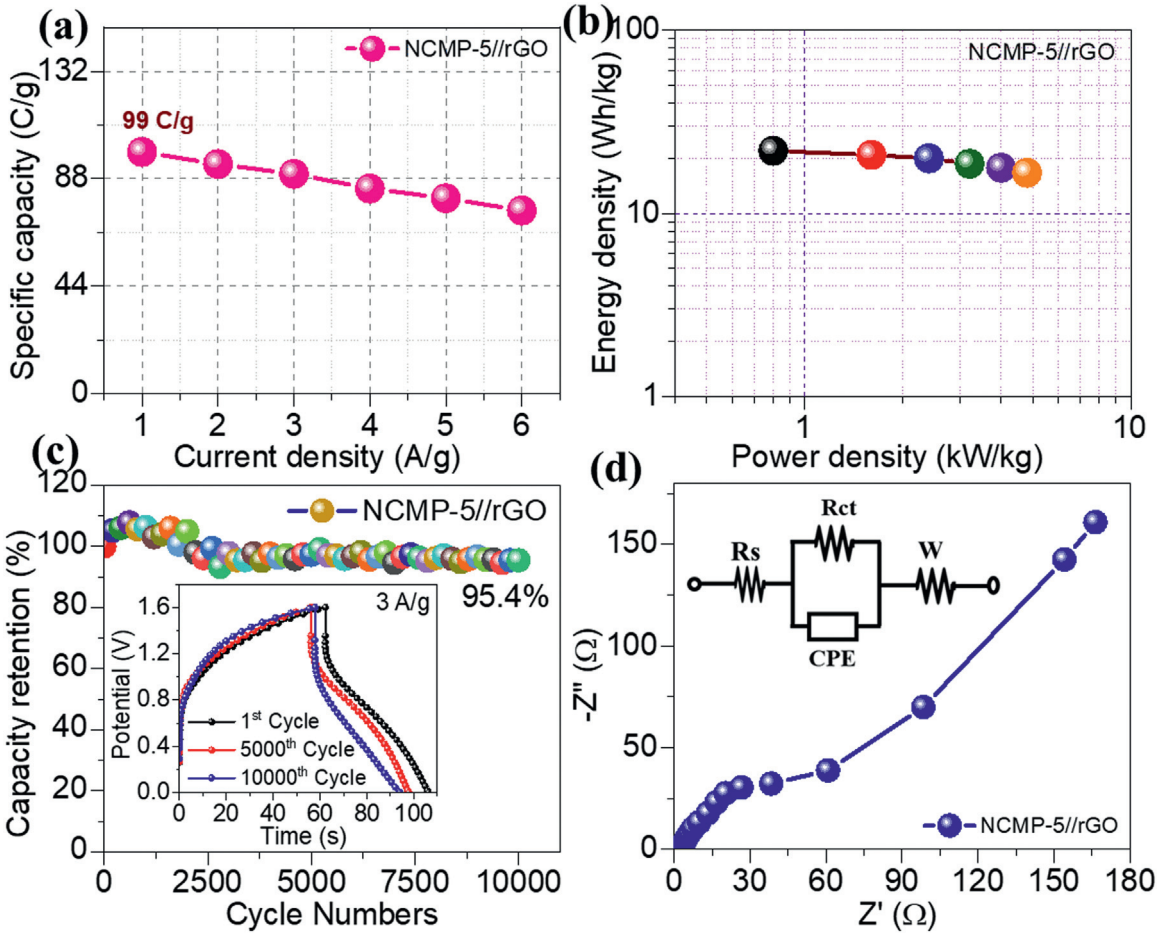

Fig. 7. (a) Plot of specific capacity vs. current density, (b) Ragone plot, (c) stability graph for 10,000 cycles [inset: 1st, 5000th, and 10000th GCD cycles], and (d) Nyquist plot [Inset: fitted equivalent circuit] of NCMP-5//rGO HSSC device.

C/g) at a higher current of 6 A/g. It is evident that the decrease in specific capacity with increasing current is attributed to the inadequate diffusion of electrolytic ion species in the porous rGO structure under high current density scenarios [14]. In addition, two essential parameters that determine the productivity of energy storage devices are power (P) and energy density (E). The (mass and volumetric) energy and power density of the NCMP-5//rGO HSSC device were calculated using Eqn (S6-S9) at different current densities, as displayed in the Ragone plot (Figs. 7(b) and S8). The NCMP-5//rGO HSSC device displays a maximum energy density of 22 Wh/kg (3.66 Wh cm^{-3}) at a power density of 0.8 kW/kg (0.133 kW/cm^3) on 1 A/g current density, whereas, at high power of 4.8 kW/kg (2.77 Wh/cm^3), the device retains an impressive energy density of 16.6 Wh/kg (0.800 kW/ cm^3) at 6 A/g. According to the Ragone plot, an assembled HSSC device displays superior energy and power values that indicate significant potential for real-world applications, and these outcomes are nearly comparable to those of other similar transition metals-based devices published in previous research works (as described in Table S2) [2,7,13-15,31,65-69].

Moreover, the long-term cyclability of the NCMP-5//rGO HSSC device was demonstrated by executing 10,000 consecutive GCD cycles at 3 A/g (Fig. 7(c)). After 10,000 GCD cycles, the fabricated HSSC device maintains high capacity retention (95.4 %) of its first recorded capacity at a specific current of 3 A/g, indicating the stability and reversibility of the device's anode and cathode materials. Even more importantly, the device sustains 99 % efficiency (inset of Fig. 7(c)) for the first 2500 cycles, with just a 4.6 % decrease following that until the completion of the 10,000 cycles. This implies that, even after 10,000 continuous cycle tests, the electrode materials in the device exhibit no substantial deterioration. Such outstanding performance is attributed to the Ni-Co-Mn phosphate, MXene, and rGO material's large porous and interconnected nanostructure, which promotes a quick charge transfer process [75]. Additionally, the improved cycle stability value for the NCMP-5//rGO HSSC device is further compared with other hybrid transition metals-based devices that have been documented in the literature (in Table S2) [2,7,13-15,31,65-69].

After that, Fig. 7(d) depicts an EIS Nyquist graph of the HSSC device employed to evaluate the Ohmic and charge transfer resistances (diffusion kinetics) on its electrode surfaces in a gel electrolyte [76]. Also, the corresponding circuit fitting of this device is illustrated in the inset of Fig. 7(d). According to the Nyquist plot, the equivalent series resistance (R_S) is determined to be 1.7 Ω, suggesting that the gel solution and device electrode materials recovered efficiently and achieved higher conductivity. Furthermore, the device displays a small semicircle in the high-frequency range (R_{ct} = 80.5 Ω), indicating a low charge transfer resistance and quick mass transfer between its electrodes and the gel electrolyte, verifying the rapid charge/discharge capabilities of the constructed device.

To ensure the practical prospect of an HSSC device for energy storage and conversion, two HSSC devices are connected in series as a power supply that illuminates different colored light-emitting diodes (LEDs), as demonstrated in Fig. 8(a–h). The operational voltage windows of these two serially connected HSSC (each with a voltage of +1.6 V) devices reach +3.2 V. Therefore, after charging these paired devices for 30 s, a commercial white, green, red, and yellow colored LED glowed for 110, 150, 180, and 215 s, respectively. This study confirms that the NCMP-5-based cathode has demonstrated high specific energy and power capabilities, showing the outstanding perspective of the constructed HSSC device for energy-storage applications. These results suggest that the rational fabrication of trimetallic Ni-Co-Mn phosphate with the addition of MXene improves the electrochemical efficiency, which has tremendous potential for application in cutting-edge energy storage devices.

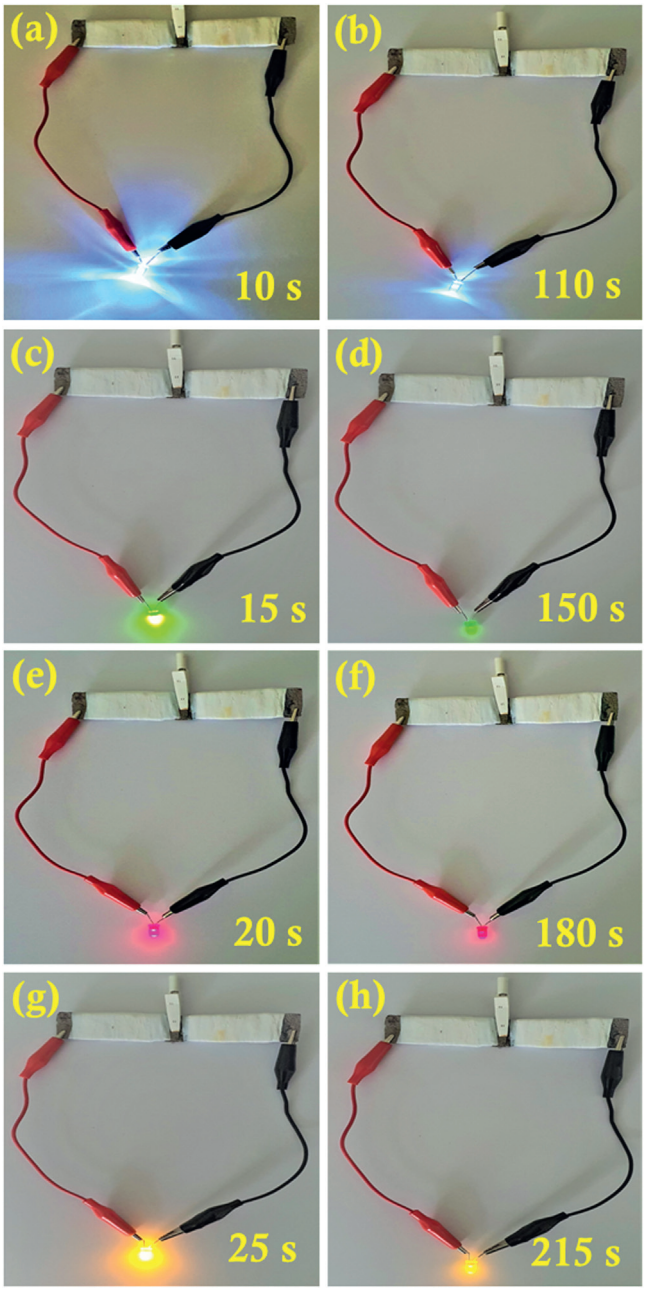

Fig. 8. Demonstration photographs of the NCMP-5//rGO HSSC device by illuminating (a, b) White, (c, d) Green, (e, f) Red, and (g, h) Yellow LED's.

4. Conclusions

In summary, we successfully designed a unique 3D@2D structure of amorphous Ni-Co-Mn phosphate@$Ti_3C_2T_x$ nanocomposites. In the synthesis process, MXene nanosheets were effectively deposited onto NF using the drop-casting approach, followed by its composites with the Ni-Co-Mn phosphate nanostructure through the electrodeposition technique. Aside from the synergistic impact that resulted from integrating MXene with the ternary transition metals, the porous nano-structural design and the 2D/3D networks improved the storage capacity performance by enabling redox-active site access, increasing the active surface area, and

promoting rapid ion transportation. Furthermore, the charge storage mechanism analysis of the NCMP-5 sample revealed a combination of both diffusion-controlled and surface-controlled processes. Among the as-prepared samples, NCMP-5 exhibits the highest specific capacity of 342 mAh/g (1230 C/g) at 5.0 A/g current density, which is higher than that of the pristine samples. Moreover, the capacity retention of NCMP-5 reached 98.8 % after 5000 GCD cycles. In addition, the NCMP-5//rGO HSSC device was designed for real-world application by employing NCMP-5 as the cathode and rGO as the anode in the PVA-KOH solid gel electrolyte. Impressively, the assembled HSSC device delivered a high specific capacity of 27.5 mAh/g (99 C/g) with a high (volumetric) energy density of 22 Wh/kg (3.6 Wh/cm^3) and a power density of 4.8 kW/kg (0.13 kW/cm^3), alongside retained $\sim$ 95.4 % of its initial capacity even after 10,000 cycles. Furthermore, the two serially connected HSSC devices effectively illuminated different colored LEDs. Our findings reveal a synergy effect between transition metals (Ni-Co-Mn) phosphate and MXene, exploiting a new opportunity to enhance charge storage performance and develop novel electro-active materials in future studies.

Declaration of competing interest

The authors declare that they have no known competing financial interests or personal relationships that could have appeared to influence the work reported in this paper.

CRediT authorship contribution statement

Pranav K. Katkar: Methodology, Writing – original draft, Conceptualization, Formal analysis. **Zulfqar Ali Sheikh:** Data curation, Validation. **Vijay D. Chavan:** Data curation, Validation, Visualization. **Sang-Wha Lee:** Funding acquisition, Project administration, Resources, Supervision, Writing – review & editing.

Acknowledgement

This research was supported by the National Research Foundation of Korea (NRF) (NRF-2021R1A2C1005867). This research was also supported by the Basic Science Research Program through the National Research Foundation of Korea (NRF) funded by the Ministry of Education (2021R1A6A1A03038996).

Supplementary materials

Supplementary material associated with this article can be found, in the online version, at doi:10.1016/j.jmst.2024.03.044.

References

[1] Z.A. Sheikh, P.K. Katkar, H. Kim, S. Rehman, K. Khan, V.D. Chavan, R. Jose, M.F. Khan, D.K. Kim, J. Energy Storage 71 (2023) 107997.
[2] Y. Wang, F. Xu, L. Sun, S. Fang, J. Lao, C. Zhang, S. Wei, L. Liao, Y. Guan, Y. Xia, Y. Luo, Y. Sun, Y. Zou, Z. Yu, Q. Shao, Y. Zhu, Y. Luo, J. Energy Storage 58 (2023) 106395.
[3] K.V. Sankar, Y. Seo, S.C. Lee, S. Liu, A. Kundu, C. Ray, S.C. Jun, Electrochim. Acta 259 (2018) 1037–1044.
[4] H. Wang, Z. Xu, Z. Li, K. Cui, J. Ding, A. Kohandehghan, X. Tan, B. Zahiri, B.C. Olsen, C.M.B. Holt, D. Mitlin, Nano Lett. 14 (2014) 1987–1994.
[5] Z. Zhu, Z. Zhang, Q. Zhuang, F. Gao, Q. Liu, X. Zhu, M. Fu, J. Power Sources 492 (2021) 229669.
[6] M.R. Lukatskaya, B. Dunn, Y. Gogotsi, Nat. Commun. 7 (2016) 12647.
[7] Y. Yang, Y. Zhou, Z. Hu, W. Wang, X. Zhang, L. Qiang, Q. Wang, J. Alloy. Compd. 772 (2019) 683–692.
[8] P.K. Katkar, S.A. Patil, J.H. Jeon, H.R. Na, N.S. Padalkar, S.K. Jerng, S. Lee, S.H. Chun, Energy Fuels 36 (2022) 13356–13369.
[9] P.K. Katkar, N.S. Padalkar, A.M. Patil, J.H. Jeon, Z.A. Sheikh, S.K. Jerng, H.R. Na, S. Lee, S.H. Chun, Int. J. Energy Res. 46 (2022) 12039–12056.
[10] P.K. Katkar, S.J. Marje, S.S. Pujari, S.A. Khalate, A.C. Lokhande, U.M. Patil, ACS Sustain. Chem. Eng. 7 (2019) 11205–11218.
[11] S.J. Marje, P.K. Katkar, S.S. Pujari, S.A. Khalate, P.R. Deshmukh, U.M. Patil, Mater. Sci. Eng. B 261 (2020) 114641.
[12] P.K. Katkar, S.J. Marje, S.S. Pujari, S.A. Khalate, P.R. Deshmukh, U.M. Patil, Synth. Met. 267 (2020) 116446.
[13] M. Xie, M. Zhou, Y. Zhang, C. Du, J. Chen, L. Wan, J. Colloid Interface Sci. 608 (2022) 79–89.
[14] A.A. Saleh, A. Amer, D.M. Sayed, N.K. Allam, Electrochim. Acta 380 (2021) 138197.
[15] X. Lei, S. Ge, Y. Tan, Z. Wang, J. Li, X. Li, G. Hu, X. Zhu, M. Huang, Y. Zhu, B. Xiang, ACS Appl. Mater. Interfaces 12 (2020) 9158–9168.
[16] P.K. Katkar, A.N. Kadam, S.K. Jerng, S.H. Chun, S.W. Lee, J. Alloy. Compd. 968 (2023) 171935.
[17] L.G. Ghanem, M.M. Taha, B.S. Shaheen, N.K. Allam, ACS Appl. Mater. Interfaces (2023) 1–15.
[18] P.K. Katkar, S.J. Marje, V.G. Parale, C.D. Lokhande, J.L. Gunjakar, H.H. Park, U.M. Patil, Langmuir 37 (2021) 5260–5274.
[19] S.J. Marje, P.K. Katkar, S.S. Pujari, S.A. Khalate, A.C. Lokhande, U.M. Patil, Synth. Met. 259 (2020) 116224.
[20] P.K. Katkar, S.J. Marje, S.B. Kale, A.C. Lokhande, C.D. Lokhande, U.M. Patil, CrystEngComm 21 (2019) 884–893.
[21] K. Raju, Curr. Opin. Electrochem. 21 (2020) 351–357.
[22] A. Philip, A.R. Kumar, Sust. Energ. Rev. 182 (2023) 113423.
[23] T. Kshetri, D.T. Tran, H.T. Le, D.C. Nguyen, H.V. Hoa, N.H. Kim, J.H. Lee, Prog. Mater. Sci. 117 (2021) 100733.
[24] M. Naguib, M.W. Barsoum, Y. Gogotsi, Adv. Mater. 33 (2021) 2103393.
[25] Y. Yang, X. Huang, C. Sheng, Y. Pan, Y. Huang, X. Wang, J. Alloy. Compd. 920 (2022) 165908.
[26] S. Hussain, P.K. Katkar, D. Vikraman, Z.A. Sheikh, G. Nazir, K.M. Batoo, D.K. Kim, H.S. Kim, J. Jung, Int. J. Energy Res. (2023) 6653784.
[27] X. Li, J. Huang, L. Wang, J. Zhang, S. Song, G. Li, P. Wang, P. Sun, Y. Yang, J. Alloy. Compd. 838 (2020) 155626.
[28] Q. Shi, Q. Liu, Y. Ma, Z. Fang, Z. Liang, G. Shao, B. Tang, W. Yang, L. Qin, X. Fang, Adv. Energy Mater. 10 (2020) 1903854.
[29] M. Xie, S. Duan, Y. Shen, K. Fang, Y. Wang, M. Lin, X. Guo, ACS Energy Lett. 1 (2016) 814–819.
[30] M. Xie, Z. Xu, S. Duan, Z. Tian, Y. Zhang, K. Xiang, M. Lin, X. Guo, W. Ding, Nano Res. 11 (2018) 216–224.
[31] L. He, G. Wang, N. ur R. Lashari, Z. Guo, M. Li, ACS Appl. Nano Mater. 6 (2023) 16400–16413.
[32] G.W. Yang, C.L. Xu, H.L. Li, Chem. Commun. (2008) 6537–6539.
[33] T. Jiang, Y. Zhang, C. Du, T. Xiao, L. Wan, J. Colloid Interface Sci. 629 (2023) 1049–1060.
[34] M. Zhang, H. Du, Z. Wei, X. Zhang, R. Wang, ACS Appl. Energy Mater. 5 (2022) 186–195.
[35] J. Hao, X. Zou, L. Feng, W. Li, B. Xiang, Q. Hu, X. Liang, Q. Wu, J. Colloid Interface Sci. 583 (2021) 243–254.
[36] A. Roy, H.S. Jadhav, J.G. Seo, Electroanalysis 33 (2021) 705–712.
[37] A.C. Khot, T.D. Dongale, J.H. Park, A.V. Kesavan, T.G. Kim, ACS Appl. Mater. Interfaces 13 (2021) 5216–5227.
[38] M. Chandran, A. Raveendran, M. Vinoba, B.K. Vijayan, M. Bhagiyalakshmi, Ceram. Int. 47 (2021) 26847–26855.
[39] X. Wang, X. Zhai, P. Lv, Y. Jiao, S. Wang, J. Chi, Synth. Met. 292 (2023) 117217.
[40] A.A. Mirghni, K.O. Oyedotun, B.A. Mahmoud, A. Bello, S.C. Ray, N. Manyala, Compos. Pt. B-Eng. 174 (2019) 106953.
[41] R.A. Nyquist, R.O. Kagel, in: Handbook of Infrared and Raman spectra of Inorganic Compounds and Organic salts: Infrared Spectra of Inorganic Compounds, Academic Press, New York, 2012, pp. 1–17.
[42] H. Shao, N. Padmanathan, D. McNulty, C. O'Dwyer, K.M. Razeeb, ACS Appl. Mater. Interfaces 8 (2016) 28592–28598.
[43] P. Arunkumar, S. Gayathri, D. Saha, J.H. Han, J. Colloid Interface Sci. 635 (2023) 562–577.
[44] M.V. Tran, A.T. Ha, P.M.L. Le, J. Nanomater. 2015 (2015) 609273.
[45] A.A. Mirghni, M.J. Madito, K.O. Oyedotun, T.M. Masikhwa, N.M. Ndiaye, Sekhar.J. Ray, N. Manyala, RSC Adv. 8 (2018) 11608–11621.
[46] M.N. Mustafa, M.A.A.M. Abdah, A. Numan, Y. Sulaiman, R. Walvekar, M. Khalid, J. Energy Storage 68 (2023) 107880.
[47] D. Zhao, R. Zhao, S. Dong, X. Miao, Z. Zhang, C. Wang, L. Yin, Energy Environ. Sci. 12 (2019) 2422–2432.
[48] T. Hu, J. Wang, H. Zhang, Z. Li, M. Hu, X. Wang, Phys. Chem. Chem. Phys. 17 (2015) 9997–10003.
[49] R. Liu, W. Li, ACS Omega 3 (2018) 2609–2617.
[50] H. Zhang, Z. Li, Z. Hou, H. Mei, Y. Feng, B. Xu, D. Sun, Chem. Eng. J. 425 (2021) 130602.
[51] A. Mateen, M.Z. Ansari, Q. Abbas, A. Muneeb, A. Hussain, E.T. Eldin, F.M. Alzahrani, N.S. Alsaiari, S. Ali, M.S. Javed, Molecules 27 (2022) 7446.
[52] B. Ahmed, D.H. Anjum, M.N. Hedhili, Y. Gogotsi, H.N. Alshareef, Nanoscale 8 (2016) 7580–7587.
[53] O. Gerard, A. Numan, M. Khalid, S. Ramesh, K. Ramesh, J. Alloy. Compd. 941 (2023) 168878.
[54] R. Li, C. Liu, P. Tang, B. Yang, X. Li, G. Yang, L. Xie, Vacuum 192 (2021) 110395.
[55] M. Li, M. Zhao, S. Mourdikoudis, Q. Zheng, L. Jiao, Z. Su, M. Shi, Q. Wang, Y. Wu, S. Yang, J. Power Sources 580 (2023) 233333.
[56] W. Luo, Y. Sun, Y. Han, J. Ding, T. Li, C. Hou, Y. Ma, Electrochim. Acta 441 (2023) 141818.
[57] A.K. Singh, D. Sarkar, K. Karmakar, K. Mandal, G.G. Khan, ACS Appl. Mater. Interfaces 8 (2016) 20786–20792.
[58] W. Wu, C. Zhao, D. Niu, J. Zhu, D. Wei, C. Wang, L. Wang, L. Yang, Appl. Surf. Sci. 539 (2021) 148272.

[59] Y. Wang, F. Xu, F. Zhou, L. Dai, K. Qu, Y. Wu, S. Gu, Z. Xu, Ind. Eng. Chem. Res. 61 (2022) 8800–8808.
[60] T. Yu, S. Li, L. Zhang, F. Li, J. Wang, H. Pan, D. Zhang, J. Colloid Interface Sci. 629 (2023) 546–558.
[61] N. Zhao, Y. Feng, H. Chen, Electrochim. Acta 441 (2023) 141756.
[62] Y. Du, G. Li, L. Ye, C. Che, X. Yang, L. Zhao, Chem. Eng. J. 417 (2021) 129189.
[63] D. Jiang, C.Y. Wei, Z.Y. Zhu, X.H. Guan, M. Lu, X.J. Zhang, G.S. Wang, Inorg. Chem. Front. 8 (2021) 4324–4333.
[64] Z. Andikaey, A.A. Ensafi, B. Rezaei, Electrochim. Acta 393 (2021) 139061.
[65] C. Deng, J. He, G. Wang, K. Wang, W. Dong, X. Hong, Appl. Surf. Sci. 616 (2023) 156526.
[66] M.Z. Iqbal, J. Khan, H.T.A. Awan, M. Alzaid, A.M. Afzal, S. Aftab, Dalton Trans. 49 (2020) 16715–16727.
[67] X. Liu, J. Wang, N. Hu, J. Liao, N. Zong, J. Wei, M. Li, L. Wang, R. Xu, L. Yang, J. Electroanal. Chem. 932 (2023) 117262.
[68] Z.H. Xu, S.S. Sun, X.L. Li, Z.H. Zhang, H.Y. Li, S.T. Ruan, S.G. Yin, Rare Metals 43 (2024) 148–163.
[69] J. Zhao, M. Li, J. Li, C. Wei, Y. He, Y. Huang, Q. Li, Appl. Surf. Sci. 425 (2017) 1158–1167.
[70] X. Wu, B. Huang, Q. Wang, Y. Wang, Chem. Eng. J. 380 (2020) 122456.
[71] L. Zhu, C.K.N. Peh, T. Zhu, Y.F. Lim, G.W. Ho, J. Mater. Chem. A 5 (2017) 8343–8351.
[72] J. Cao, Y. Hu, Y. Zhu, H. Cao, M. Fan, C. Huang, K. Shu, M. He, H.C. Chen, Chem. Eng. J. 405 (2021) 126928.
[73] F. Barzegar, A.A. Khaleed, F.U. Ugbo, K.O. Oyeniran, D.Y. Momodu, A. Bello, J.K. Dangbegnon, N. Manyala, AIP Adv. 6 (2016) 115306.
[74] G. Wang, Z. Jin, W. Zhang, Dalton Trans. 48 (2019) 14853–14863.
[75] F. Barzegar, A. Bello, D. Momodu, M.J. Madito, J. Dangbegnon, N. Manyala, J. Power Sources 309 (2016) 245–253.
[76] M. Samir, N. Ahmed, M. Ramadan, N.K. Allam, ACS Sustain. Chem. Eng. 7 (2019) 13471–13480.